

Molecular Dynamics Simulation of Bombardment of Hydrogen Atoms on Graphite Surface

A. Ito^{1,*} and H. Nakamura²

¹ Department of Physics, Graduate School of Science, Nagoya University, Furo-cho, Chikusa-ku, Nagoya 464-8602, Japan.

² Department of Simulation Science, National Institute for Fusion Science, 322-6 Oroshi-cho, Toki 509-5292, Japan.

Received 1 November 2007; Accepted (in revised version) 10 March 2008

Available online 17 April 2008

Abstract. The new potential model of interlayer intermolecular interaction was proposed to represent "ABAB" stacking of graphite. The bombardment of hydrogen atoms on the graphite surface was investigated using molecular dynamics simulation. Before the first graphene from the surface side was broken, the hydrogen atoms caused the following processes. In the case of the incident energy of 5 eV, many hydrogen atoms were adsorbed on the front of the first graphite. In the case of the incident energy of 15 eV, almost all hydrogen atoms were reflected by the first graphene. In the case of the incident energy of 30 eV, the hydrogen atoms were adsorbed between the first and second graphenes. The radial distribution function and the animation of the MD simulation demonstrated that the graphenes were peeled off one by one, which is called graphite peeling. One C₂H₂ was generated in such chemical sputtering. But the other yielded molecules often had chain structures terminated by the hydrogen atoms. The erosion yield increased linearly with time.

PACS: 52.55.Rk, 52.65.Yy, 52.77.Bn, 81.05.Uw, 83.10.Mj

Key words: Plasma surface interaction, chemical sputtering, graphite, graphene, hydrogen atom.

1 Introduction

In the research into nuclear fusion, we deal with the plasma surface interaction (PSI) problem [1–7]. In the experiment of plasma confinement, a portion of hydrogen plasma flows into the divertor walls, which are shielded by the tiles of polycrystalline graphite or carbon fiber composite. The hydrogen plasma which has weak incident energy erodes

*Corresponding author. *Email addresses:* ito.atsushi@nifs.ac.jp (A. Ito), nakamura.hiroaki@nifs.ac.jp (H. Nakamura)

these carbon tiles. This process is called chemical sputtering. The erosion produces hydrocarbon molecules, such as CH_x and C_2H_x . The hydrocarbon molecules affect the plasma confinement. The PSI has been researched using molecular dynamics simulation (MD) [8–11].

The authors have performed the MD simulation of the PSI on graphite surface using the modified Brenner reactive empirical bond order (REBO) potential [12]. From the MD simulation, it is shown that if incident energy is 5 eV, the surface of the graphite absorbs many hydrogen atoms, while if the incident energy is 15 eV, almost all of hydrogen atoms are reflected by the surface. These absorption and reflection occur on the first graphene from the surface of the graphite. This behavior appeared in the case of deuterium and tritium injection also [13]. The absorption and reflection on the first graphene layer could be explained by the MD simulation of the chemical interaction between a single hydrogen atom and a single graphene [14–16]. The MD simulation revealed that the hydrogen atom with the incident energy of more than 20 eV could penetrate the first graphene from the surface of the graphite. This penetration relates to the intercalation of the hydrogen atoms between the graphite layers. However, in the MD simulation of the graphite, the intercalation between graphite layers did not appear. To be precise, the layer structure of the graphite was broken as soon as the hydrogen atoms dived under the graphite surface. Because the incident hydrogen atoms pushed the graphite surface, covalent bonds between the first and second graphenes occur. The graphenes bound by the covalent bonds change into an amorphous structure. This was the trigger of the graphite erosion.

The above MD simulation did not include the interlayer intermolecular interaction of the graphite. If the interlayer intermolecular interaction is adopted, the above dynamics changes. However, the interlayer intermolecular interaction of the graphite has not been clarified enough. For example, the existing potential model of the interlayer intermolecular interaction for the MD simulation does not deal with “ABAB” stacking of the graphite structure. Before we look into the effect of the interlayer intermolecular interaction, we need to create a new potential model of the interlayer intermolecular interaction.

We enrich the MD simulation of the bombardment of the hydrogen atoms on the graphite surface with the interlayer intermolecular interaction. In Section 2, we denote the modified Brenner REBO potential and the potential model of the interlayer intermolecular interaction. The simulation model is described in Section 3. Simulation results are shown in Section 4 and discussed in Section 5. This paper concludes with a Section 6.

2 Potential models

2.1 Modified Brenner REBO potential model

We describe the model of Brenner reactive empirical bond order (REBO) potential [17] and our modification points. This potential model is created based on Morse potential [18], Abell potential [19] and Tersoff potential [20,21].

The potential function U is defined by

$$U \equiv \sum_{i,j>i} \left[V_{[ij]}^R(r_{ij}) - \bar{b}_{ij}(\{r\}, \{\theta^B\}, \{\theta^{DH}\}) V_{[ij]}^A(r_{ij}) \right], \quad (2.1)$$

where r_{ij} is the distance between the i -th and j -th atoms. The bond angle θ_{jik}^B is the angle between the vector from the i -th atom to the j -th atom and the vector from the i -th atom to the k -th atom as follows:

$$\cos \theta_{jik}^B = \frac{\vec{x}_{ji} \cdot \vec{x}_{ki}}{r_{ji} r_{ki}}, \quad (2.2)$$

where $\vec{x}_{ij} \equiv \vec{x}_i - \vec{x}_j$ is the relative vector of position coordinate from the j -th atom to the i -th atom. The dihedral angle θ_{kijl}^{DH} is the angle between the plane through the j -th, i -th and k -th atoms and the plane through the i -th, j -th and l -th atoms. The cosine function of θ_{kijl}^{DH} is given by

$$\cos \theta_{kijl}^{DH} = \frac{\vec{x}_{ik} \times \vec{x}_{ji} \cdot \vec{x}_{ji} \times \vec{x}_{lj}}{r_{ik} r_{ji} r_{ji} r_{lj}}. \quad (2.3)$$

The repulsive function $V_{[ij]}^R(r_{ij})$ and the attractive function $V_{[ij]}^A(r_{ij})$ are defined by

$$V_{[ij]}^R(r_{ij}) \equiv f_{[ij]}^c(r_{ij}) \left(1 + \frac{Q_{[ij]}}{r_{ij}} \right) A_{[ij]} \exp(-\alpha_{[ij]} r_{ij}), \quad (2.4)$$

$$V_{[ij]}^A(r_{ij}) \equiv f_{[ij]}^c(r_{ij}) \sum_{n=1}^3 B_{n[ij]} \exp(-\beta_{n[ij]} r_{ij}). \quad (2.5)$$

The square brackets $[ij]$ mean that each function and each parameter depends only on the species of the i -th and j -th atoms, for example V_{CC}^R , V_{HH}^R and $V_{CH}^R (= V_{HC}^R)$.

The cutoff function $f_{[ij]}^c(r_{ij})$ determines effective ranges of the covalent bond between two atoms. The cutoff function $f_{[ij]}^c(r_{ij})$ indicates the presence of the covalent bond between the two atoms. The two atoms are bound by the covalent bond if the distance r_{ij} is shorter than $D_{[ij]}^{\min}$. Two atoms are not bound by the covalent bond if the distance r_{ij} is longer than $D_{[ij]}^{\max}$. The cutoff function $f_{[ij]}^c(r_{ij})$ connects the above two states smoothly as

$$f_{[ij]}^c(x) \equiv \begin{cases} 1 & (x \leq D_{[ij]}^{\min}), \\ \frac{1}{2} \left[1 + \cos \left(\pi \frac{x - D_{[ij]}^{\min}}{D_{[ij]}^{\max} - D_{[ij]}^{\min}} \right) \right] & (D_{[ij]}^{\min} < x \leq D_{[ij]}^{\max}), \\ 0 & (x > D_{[ij]}^{\max}). \end{cases} \quad (2.6)$$

The constants $D_{[ij]}^{\min}$ and $D_{[ij]}^{\max}$ depend on the species of the two atoms (Table 1).

Table 1: The constants for the cutoff function $f_{[ij]}^c(r_{ij})$. They depend on the species of the i -th and the j -th atoms.

[ij]	$D_{[ij]}^{\min}$ (Å)	$D_{[ij]}^{\max}$ (Å)
CC	1.7	2.0
CH	1.3	1.8
HH	1.1	1.7

The functions $V_{[ij]}^R$ and $V_{[ij]}^A$ in Eq. (2.1) generate two-body forces, because both are functions of the distance r_{ij} only. A multi-body force is used instead of the effect of an electron orbital. In this model, $\bar{b}_{ij}(\{r\}, \{\theta^B\}, \{\theta^{DH}\})$ in Eq. (2.1) gives a multi-body force defined by

$$\bar{b}_{ij}(\{r\}, \{\theta^B\}, \{\theta^{DH}\}) \equiv \frac{1}{2} \left[b_{ij}^{\sigma-\pi}(\{r\}, \{\theta^B\}) + b_{ji}^{\sigma-\pi}(\{r\}, \{\theta^B\}) \right] + \Pi_{ij}^{RC}(\{r\}) + b_{ij}^{DH}(\{r\}, \{\theta^{DH}\}). \quad (2.7)$$

The first term $\frac{1}{2}[\dots]$ generates a three-body force mainly. The second term Π_{ij}^{RC} in Eq. (2.7) represents the influence of radical energetics and π bond conjugation [17]. The third term $b_{ij}^{DH}(\{r\}, \{\theta^{DH}\})$ in Eq. (2.7) derives four-body force relative to the dihedral angle. Because these functions include the production of cutoff functions $f_{[ij]}^c(r_{ij})$, five- or more-body forces are generated during chemical reactions.

The function $b_{ij}^{\sigma-\pi}(\{r\}, \{\theta^B\})$ in Eq. (2.7) is defined by

$$b_{ij}^{\sigma-\pi}(\{r\}, \{\theta^B\}) \equiv \left[1 + \sum_{k \neq i, j} f_{[ij]}^c(r_{ij}) \tilde{G}_i(\cos \theta_{jik}^B) e^{\lambda_{[ijk]}} + P_{[ij]}(N_{ij}^H, N_{ij}^C) \right]^{-\frac{1}{2}}. \quad (2.8)$$

The function \tilde{G}_i in Eq. (2.8) depends on the species of the i -th atom. If $\cos \theta_{jik}^B > \cos(109.47^\circ)$ and the i -th atom is carbon, \tilde{G}_i is defined by

$$\tilde{G}_i(\cos \theta_{jik}^B) \equiv [1 - Q_c(M_i^t)] G_C(\cos \theta_{jik}^B) + Q_c(M_i^t) \gamma_C(\cos \theta_{jik}^B). \quad (2.9)$$

If $\cos \theta_{jik}^B \leq \cos(109.47^\circ)$ and the i -th atom is carbon, \tilde{G}_i is defined by

$$\tilde{G}_i(\cos \theta_{jik}^B) \equiv G_C(\cos \theta_{jik}^B). \quad (2.10)$$

And, if the i -th atom is hydrogen, \tilde{G}_i is defined by

$$\tilde{G}_i(\cos \theta_{jik}^B) \equiv G_H(\cos \theta_{jik}^B). \quad (2.11)$$

Here G_C , γ_C and G_H are the sixth order polynomial spline functions. Though the spline function \tilde{G}_i needs seven coefficients, only six coefficients are written in Brenner's paper

Table 2: The parameters for the sixth order spline function $G_C(\cos\theta_{jik}^B)$.

$\cos\theta_{jik}^B$	G_C	G'_C	G''_C	$G_C^{(3)}$
-1	-0.001	0.10400	0	0
-1/2	0.05280	0.170	0.370	-5.232
$\cos(109.47^\circ)$	0.09733	0.400	1.980	41.6140
1	8.0	0.23622	-166.1360	—

Table 3: The parameters for the sixth order spline function $\gamma_C(\cos\theta_{jik}^B)$.

$\cos\theta_{jik}^B$	γ_C	γ'_C	γ''_C	$\gamma_C^{(3)}$
$\cos(109.47^\circ)$	0.09733	0.400	1.980	-9.9563027
1	1.0	0.78	-11.3022275	—

Table 4: The parameters for the sixth order spline function $G_H(\cos\theta_{jik}^B)$. The parameters are determined under $\cos\theta_{jik}^B = 0$.

Parameter	$G_H(0)$	$G'_H(0)$	$G''_H(0)$	$G_H^{(3)}(0)$	$G_H^{(4)}(0)$	$G_H^{(5)}(0)$	$G_H^{(6)}(0)$
Value	19.06510	1.08822	-1.98677	8.52604	-6.13815	-5.23587	4.67318

[17]. We determine the seven coefficients in Tables 2, 3 and 4, respectively. The function Q_c and the coordination number M_i^t in Eq. (2.9) are defined by

$$Q_c(x) \equiv \begin{cases} 1 & (x \leq 3.2), \\ \frac{1}{2}[1 + \cos(2\pi(x - 3.2))] & (3.2 < x \leq 3.7), \\ 0 & (x > 3.7), \end{cases} \quad (2.12)$$

$$M_i^t \equiv \sum_{k \neq i} f_{[ik]}^c(r_{ik}). \quad (2.13)$$

The constant $\lambda_{[ijk]}$ in Eq. (2.8) is a weight of the three-body force. In comparison with Brenner's former potential [22], we set the constants $\lambda_{[ijk]}$ as follows:

$$\lambda_{HHH} = 4.0, \quad (2.14)$$

$$\begin{aligned} \lambda_{CCC} &= \lambda_{CCH} = \lambda_{CHC} = \lambda_{HCC} \\ &= \lambda_{HHC} = \lambda_{HCH} = \lambda_{CHH} = 0. \end{aligned} \quad (2.15)$$

The function $P_{[ij]}$ in Eq. (2.8) is necessary for solid structures. The function $P_{[ij]}$ is the bicubic spline function which depends on the parameters in Table 5. The variables N_{ij}^H and N_{ij}^C are, respectively, the numbers of hydrogen and carbon atoms bound with the i -th

Table 5: Parameters for the bicubic spline function $P_{[ij]}(N_{ij}^H, N_{ij}^C)$. The parameters which are not denoted are zero.

$P_{[ij]}(N_{ij}^H, N_{ij}^C)$	Value	$P_{[ij]}(N_{ij}^H, N_{ij}^C)$	Value
$P_{CC}(1,1)$	0.003026697473481	$P_{CH}(3,0)$	-0.303927546346162
$P_{CC}(2,0)$	0.007860700254745	$P_{CH}(0,1)$	0.01
$P_{CC}(3,0)$	0.016125364564267	$P_{CH}(0,2)$	-0.1220421462782555
$P_{CC}(1,2)$	0.003179530830731	$P_{CH}(1,1)$	-0.1251234006287090
$P_{CC}(2,1)$	0.006326248241119	$P_{CH}(2,1)$	-0.298905245783
$P_{CH}(1,0)$	0.2093367328250380	$P_{CH}(0,3)$	-0.307584705066
$P_{CH}(2,0)$	-0.0644449615432525	$P_{CH}(1,2)$	-0.3005291724067579

atom as follows:

$$N_{ij}^H \equiv \sum_{k \neq i,j}^{\text{hydrogen}} f_{[ik]}^c(r_{ik}), \quad (2.16)$$

$$N_{ij}^C \equiv \sum_{k \neq i,j}^{\text{carbon}} f_{[ik]}^c(r_{ik}). \quad (2.17)$$

The second term Π_{ij}^{RC} in Eq. (2.7) is defined by a tricubic spline function $F_{[ij]}$ as

$$\Pi_{ij}^{\text{RC}}(\{r\}) \equiv F_{[ij]}(N_{ij}^t, N_{ji}^t, N_{ij}^{\text{conj}}), \quad (2.18)$$

where the variables are defined by

$$N_{ij}^t \equiv \sum_{k \neq i,j} f_{[ik]}^c(r_{ik}), \quad (2.19)$$

$$N_{ij}^{\text{conj}} \equiv 1 + \sum_{k(\neq i,j)}^{\text{carbon}} f_{[ik]}^c(r_{ik}) C_N(N_{ki}^t) + \sum_{l(\neq j,i)}^{\text{carbon}} f_{[jl]}^c(r_{jl}) C_N(N_{lj}^t), \quad (2.20)$$

with

$$C_N(x) \equiv \begin{cases} 1 & (x \leq 2), \\ \frac{1}{2}[1 + \cos(\pi(x-2))] & (2 < x \leq 3), \\ 0 & (x > 3). \end{cases} \quad (2.21)$$

The second and the third terms of the right hand of Eq. (2.20) are not squared. We note that they are squared in Brenner's original formulation [17]. By this modification, a numerical error becomes smaller than Brenner's original formulation. Table 6 shows the revised coefficients for $F_{[ij]}$.

The third term $b_{ij}^{\text{DH}}(\{r\}, \{\theta^{\text{DH}}\})$ in Eq. (2.7) is defined by

$$b_{ij}^{\text{DH}}(\{r\}, \{\theta^{\text{DH}}\}) \equiv T_{[ij]}(N_{ij}^t, N_{ji}^t, N_{ij}^{\text{conj}}) \left[\sum_{k \neq i,j} \sum_{l \neq j,i} (1 - \cos^2 \theta_{kijl}^{\text{DH}}) f_{[ik]}^c(r_{ik}) f_{[jl]}^c(r_{jl}) \right], \quad (2.22)$$

Table 6: Parameters for the tricubic spline function $F_{[ij]}$. The parameters which are not denoted are zero. The function $F_{[ij]}$ satisfies the following rules: $F_{[ij]}(N_1, N_2, N_3) = F_{[ij]}(N_2, N_1, N_3)$, $\partial_{N_1} F_{[ij]}(N_1, N_2, N_3) = \partial_{N_1} F_{[ij]}(N_2, N_1, N_3)$, $F_{[ij]}(N_1, N_2, N_3) = F_{[ij]}(3, N_2, N_3)$ if $N_1 > 3$, and $F_{[ij]}(N_1, N_2, N_3) = F_{[ij]}(N_1, N_2, 5)$ if $N_3 > 5$, where $\partial_{N_i} \equiv \partial / \partial N_i$.

Function	Variables			Value
	N_1	N_2	N_3	
$F_{CC}(N_1, N_2, N_3)$	1	1	1	0.105000
	1	1	2	-0.0041775
	1	1	3 to 5	-0.0160856
	2	2	1	0.09444957
	2	2	2	0.04632351
	2	2	3	0.03088234
	2	2	4	0.01544117
	2	2	5	0.0
	0	1	1	0.04338699
	0	1	2	0.0099172158
	0	2	1	0.0493976637
	0	2	2	-0.011942669
	0	3	1 to 5	-0.119798935
	1	2	1	0.0096495698
	1	2	2	0.030
	1	2	3	-0.0200
	1	2	4 to 5	-0.030133632
	1	3	2 to 5	-0.124836752
	2	3	1 to 5	-0.044709383
	$\partial_{N_1} F_{CC}(N_1, N_2, N_3)$	2	1	1
2		1	3 to 5	-0.054376
2		3	1	0.0
2		3	2 to 5	0.062418
$\partial_{N_3} F_{CC}(N_1, N_2, N_3)$	2	2	4	-0.006618
	1	1	2	-0.060543
	1	2	3	-0.020044
$F_{HH}(N_1, N_2, N_3)$	1	1	1	0.249831916
$F_{CH}(N_1, N_2, N_3)$	0	2	3 to 5	-0.0090477875
	1	3	1 to 5	-0.213
	1	2	1 to 5	-0.25
	1	1	1 to 5	-0.5

Table 7: Parameters for the tricubic spline function T_{CC} . The parameters which are not denoted are zero. The function T_{CC} satisfies the following rule: $T_{CC}(N_1, N_2, N_3) = T_{CC}(N_1, N_2, 5)$ if $N_3 > 5$.

Function	Variables			Value
	N_1	N_2	N_3	
$T_{CC}(N_1, N_2, N_3)$	2	2	1	-0.070280085
	2	2	5	-0.00809675

where $T_{[ij]}$ is a tricubic spline function and has the same variables as $F_{[ij]}$ in Eq. (2.18). The coefficients for $T_{[ij]}$ are also revised due to the modified N_{ij}^{conj} (Table 7). In the present simulation, the function $T_{[ij]}$ becomes $T_{CC}(2, 2, 5)$ for a perfect crystal graphene, and becomes

$T_{CC}(2,2,3)$ or $T_{CC}(2,2,4)$ when a hydrogen atom is absorbed.

The time step should be smaller than that of general MD. To keep the numerical error small, we set 5×10^{-18} s in the present simulation because the potential model has complex form by the cutoff functions and spline functions.

2.2 Interlayer intermolecular potential

In the research for the interlayer intermolecular interaction, the binding energy has been well investigated. However, experimental results are not enough and ab-initio calculations cannot give us correct results yet [23]. Especially, the information on the repulsion of the interlayer is hardly reported. Therefore, now, we have no other choice to create the potential model artificially. We propose the new model of the interlayer intermolecular interaction of the graphite.

First, simple intermolecular potential function between carbon atoms is defined by

$$V_{IL}(r) = A \left\{ \frac{n}{\alpha} e^{-\alpha(r/c-1)} - \left(\frac{c}{r} \right)^n \right\}, \quad (2.23)$$

where r is the distance between two carbon atoms, n is the exponent of attraction, and A, α, c are the parameters to determine binding energy. If $n > \alpha$, the potential function has a positive local maximum at $r = c$. We tried modelling the interlayer intermolecular potential using the potential of Eq. (2.23). Fig. 2(A) shows potential functions between layers which consists of the potential of Eq. (2.23). With this potential model, however, we hardly produce the difference of the potential minimum energy between the three kinds of stacking of Fig. 1. We consider that the difficulty comes from the use of only two body force.

Generally, because the attractive interaction is effective in the long range, the attractive force is substituted by a two-body force such as Lennard-Jones potential. However, because the repulsive interaction is effective in the short range, the repulsive force should not be represented by the two-body force. Especially, the repulsive interaction between the layers of the graphite is due to chemical effects. Short range chemical interaction is often represented by multi-body force in the MD simulation. Here, using the multi-body force, we propose the new model of the interlayer intermolecular potential. We note that the modified Brenner REBO potential and Brenner original model do not include the repulsive interaction between the graphite layers because their cutoff lengths are shorter than the interlayer distance of the graphite.

The product of the simple two body force $V_{IL}(r_{ij})$ of Eq. (2.23) and special cutoff function C_{ij} gives us the multi-body interaction potential:

$$U_{IL} = \sum_{i,j \neq i} C_{ij} V_{IL}(r_{ij}). \quad (2.24)$$

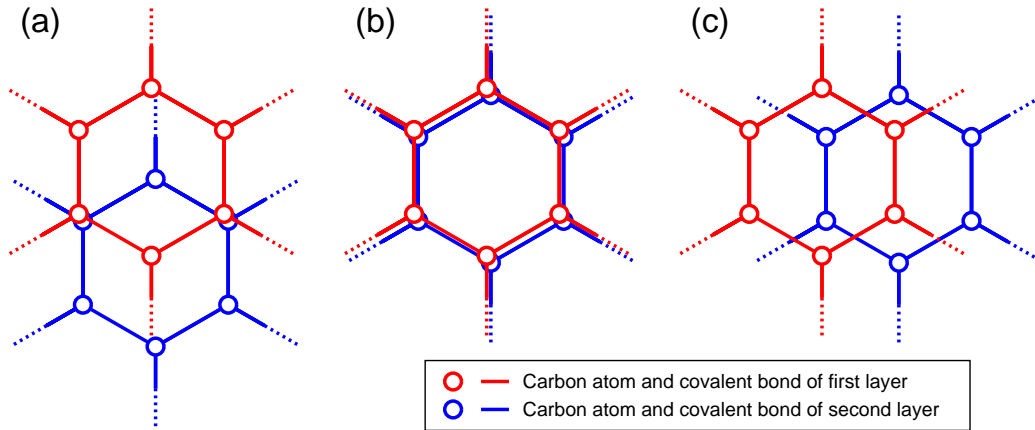


Figure 1: The three kinds of the stacking of the graphite. In general, the stable structure of the graphite is the stacking of (a).

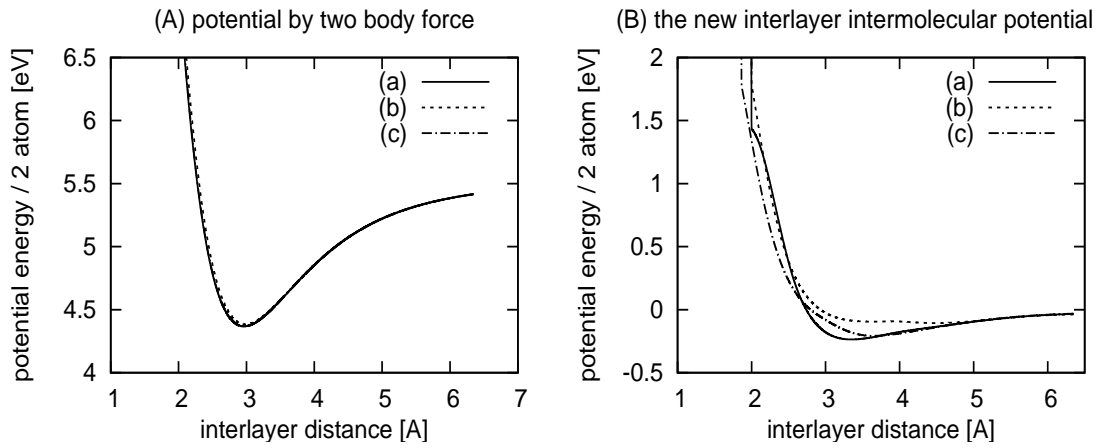


Figure 2: Interlayer intermolecular potential by using two body force only (A) and the new interlayer intermolecular potential (B). The symbols (a), (b) and (c) correspond to the three kinds of the stacking of the graphite in Fig. 1.

The special cutoff function C_{ij} depends on the angles between three atoms as

$$\begin{aligned}
 C_{ij} \equiv \frac{1}{2} \left\{ \prod_{k \neq i} \left[1 + f_{[ij]}^c(r_{ik}) \left(f^a(\cos \theta_{jik}^B) - 1 \right) \right] \right. \\
 \left. + \prod_{l \neq j} \left[1 + f_{[ij]}^c(r_{jl}) \left(f^a(\cos \theta_{jil}^B) - 1 \right) \right] \right\}, \quad (2.25)
 \end{aligned}$$

where

$$\vec{x}_{ij} \equiv \vec{x}_i - \vec{x}_j, \quad r_{ij} = |\vec{r}_{ij}|, \quad \cos \theta_{jik}^B = (\vec{x}_{ij} \cdot \vec{x}_{ik}) / (r_{ij} r_{ik}).$$

Table 8: The parameters of the potential model of the interlayer intermolecular interaction. The parameters A_{20} , A_{60} and A_{100} correspond to the coefficient A in $V_{\text{IL}}(r)$ which determines the interlayer binding energy per atom to 20 meV, 60 meV and 100 meV, respectively.

$n=6$	$\alpha=4.84$	$c=1.8 \text{ \AA}$
$A_{20}=0.9961498 \text{ eV}$	$A_{60}=2.9884494 \text{ eV}$	$A_{100}=4.980749$
$c_{\text{on}}=0.25$	$c_{\text{off}}=0.35$	

The functions $f^a(\cos\theta)$ are given by

$$f^a(\cos\theta) \equiv \begin{cases} 1 & (\cos\theta \leq c_{\text{on}}), \\ \frac{(2\cos\theta - 3c_{\text{on}} + c_{\text{off}})(\cos\theta - c_{\text{off}})^2}{(c_{\text{off}} - c_{\text{on}})^3} & (c_{\text{on}} < \cos\theta \leq c_{\text{off}}), \\ 0 & (\cos\theta > c_{\text{off}}), \end{cases} \quad (2.26)$$

where $c_{\text{on}}=0.25$ and $c_{\text{off}}=0.35$. The function $f_{[ij]}^c(r)$ is equal to the cutoff function of the modified Brenner REBO potential:

$$f_{[ij]}^c(r) \equiv \begin{cases} 1 & (r \leq D_{[ij]}^{\text{min}}), \\ \frac{1}{2} \left[1 + \cos \left(\pi \frac{r - D_{[ij]}^{\text{min}}}{D_{[ij]}^{\text{max}} - D_{[ij]}^{\text{min}}} \right) \right] & (D_{[ij]}^{\text{min}} < r \leq D_{[ij]}^{\text{max}}), \\ 0 & (r > D_{[ij]}^{\text{max}}), \end{cases} \quad (2.27)$$

where the parameters are denoted in Table 1. Now, we set the parameters α and c to keep the interlayer distance 3.35 \AA as follows: $c=1.8 \text{ \AA}$ and $\alpha=4.84$. If $A=0.9961498$, 2.9884494 and 4.980749 , the interlayer binding energy per atom becomes 20 meV, 60 meV and 100 meV, respectively (see Table 8). Fig. 2(B) shows that the new model of the interlayer intermolecular potential of Eq. (2.24) provides the difference of the minimum potential energy between the three kinds of stacking of Fig. 1. As a result, we can set the structure of "ABAB" stacking Fig. 1(a) on the most stable state.

3 Simulation method

The graphite which consists of eight graphenes [24] and has "ABAB" stacking was set to the center of coordinates parallel to x - y plane. Each graphene consisted of 160 carbon atoms measuring $2.00 \text{ nm} \times 2.17 \text{ nm}$. The size of the simulation box in the x - and y -directions is equal to that of the graphenes with periodic boundary conditions. The interlayer distance of the graphite was initially 3.35 \AA . The carbon atoms obeyed the Maxwell-Boltzmann distribution at 300 K initially. The graphenes are numbered from the surface side. During the simulation, two carbon atoms of the 8-th graphene were fixed to block the movement of whole of the graphite. One was the center atom of the 8-th graphene, and the other was located at the boundary of the 8-th graphene. The graphite surface faced the positive z -direction.

Hundreds of hydrogen atoms were injected at regular time intervals of 0.1 ps parallel to the z -axis. The flux of hydrogen atoms became $2.5 \times 10^{30} \text{s}^{-1} \text{m}^{-2}$. The z -coordinate of the injection point was 60 Å. The x - and y -coordinates of the injection point were set at random. The initial momentum vector $(0, 0, p_0)$ was defined by

$$p_0 = \sqrt{2mE_I}, \quad (3.1)$$

where E_I is the incident energy, and m is the mass of the hydrogen atom.

We adopt the *NVE* conditions, where the number of atoms, volume, and total energy are conserved, except for the addition of incident atoms and removal of outgoing atoms. The simulation time was developed using second order symplectic integration [25]. The chemical interaction was represented by the modified Brenner REBO potential. The interlayer intermolecular interaction was represented by the new model of Eq. (2.24). The interlayer binding energy was selected to 60 meV. The hydrogen atom vibrates by 1 fs in a molecule. In general, 1/100 of the vibration time, which is about 10^{-17} s in this simulation, was chosen as the time step in the MD simulation. Consequently, the particles can move along a potential surface approximately. Moreover, the modified Brenner potential complicates the potential surface that represents the chemical reaction. Therefore, as the time step, we select a half of 10^{-17} s, that is 5×10^{-18} s.

4 Results

We performed the three cases of the MD simulations in which the incident energy of all hydrogen atoms are set into 5 eV, 15 eV or 30 eV. In this section, simulation results are described with the dynamics of the hydrogen atoms.

Initially, the graphite surface was not broken. The difference between the incident energy caused the difference of hydrogen atom adsorption on the graphite surface. Figs. 3(a), 4(a) and 5(a) show the snapshots of the MD simulations at $t = 2.16$ ps, when more than 20 hydrogen atoms had undergone chemical interaction with the graphite surface. From the figures, we noticed the amount of adsorbed hydrogen atoms and adsorption sites on the graphite surface. In the case of the incident energy of 5 eV, a lot of hydrogen atoms were adsorbed by the graphite surface. The adsorption sites are at the front of the first graphene, where the graphenes are numbered from the surface side. The positive and negative side of each graphene in the direction of z are called front and backside, respectively. In the case of the incident energy of 15 eV, few hydrogen atoms were adsorbed on the graphite surface. The animation of the MD simulation illustrated that hydrogen atoms were reflected by the first graphene and went back to the positive direction of z . In the case of the incident energy of 30 eV, a lot of hydrogen atoms were adsorbed between the first and second graphene layers, that is, the backside of the first graphene or the front of the second graphene. A few hydrogen atoms are adsorbed on the front of the third graphene. The animation of the MD simulation of incidence at 30 eV demonstrated the following dynamics: A lot of hydrogen atoms passed through the first graphene, which

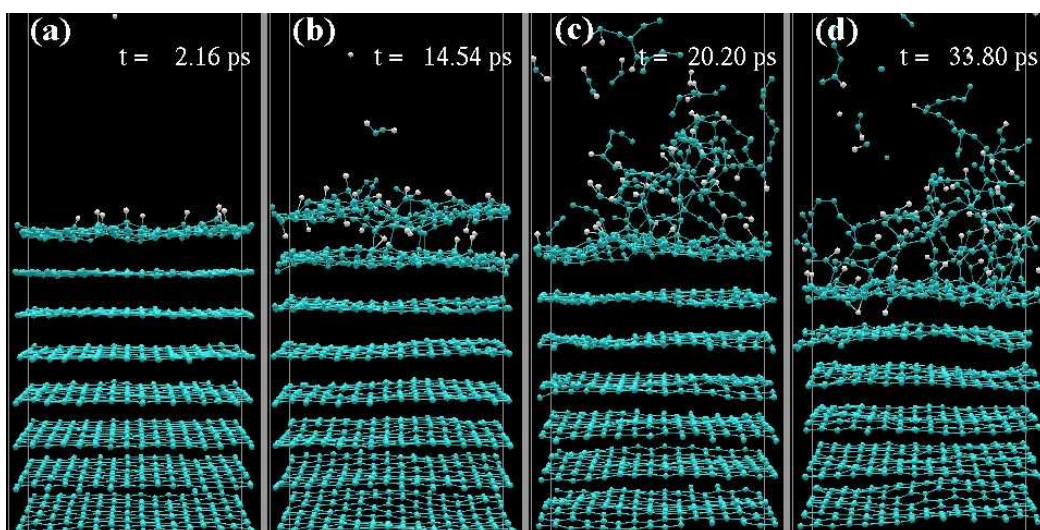


Figure 3: The snapshots of the MD simulation in the case of the incident energy of 5 eV. Green and white spheres represent carbon and hydrogen atoms, respectively.

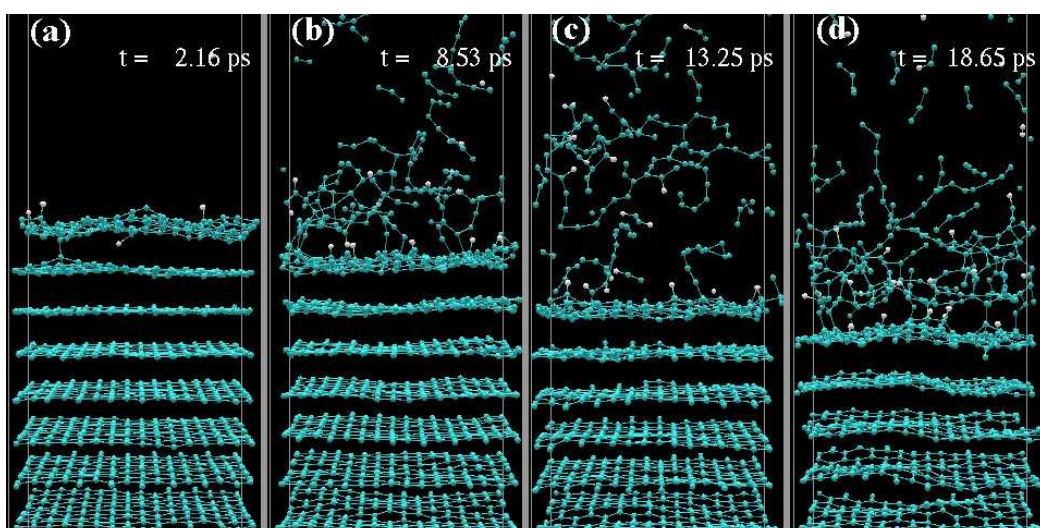


Figure 4: The snapshots of the MD simulation in the case of the incident energy of 15 eV. Green and white spheres represent carbon and hydrogen atoms, respectively.

is formed by six C-C bonds. After that, a half of them were adsorbed on the backside of the first graphene and the others flowed between the first and second graphene layers. When approaching the first or second graphene, the hydrogen atom was adsorbed. The hydrogen atoms adsorbed by the third graphene had penetrated the first and second graphene at a stretch. After the hydrogen atom penetrated into the inside of the graphite surface, it did not go out again. All of the hydrogen atoms which were not adsorbed by

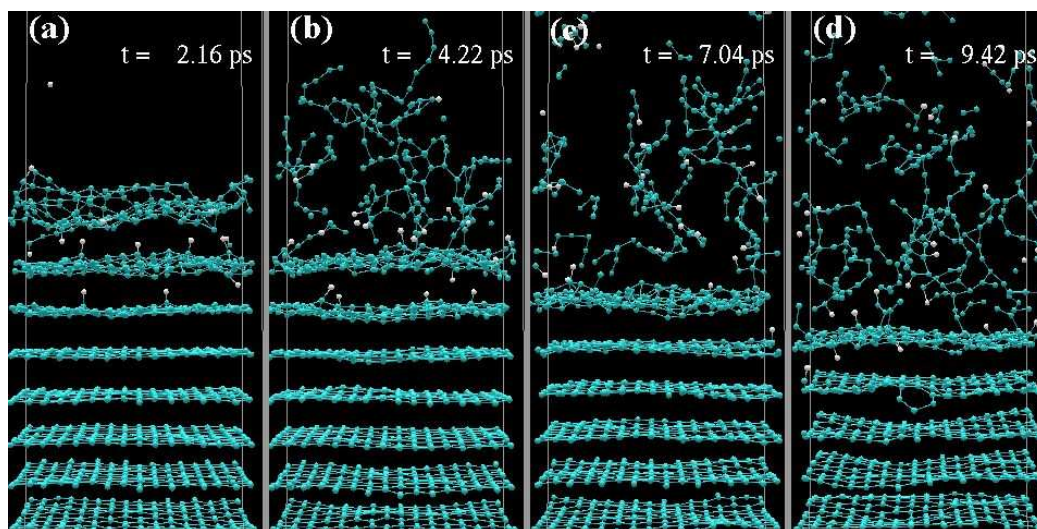


Figure 5: The snapshots of the MD simulation in the case of the incident energy of 30 eV. Green and white spheres represent carbon and hydrogen atoms, respectively.

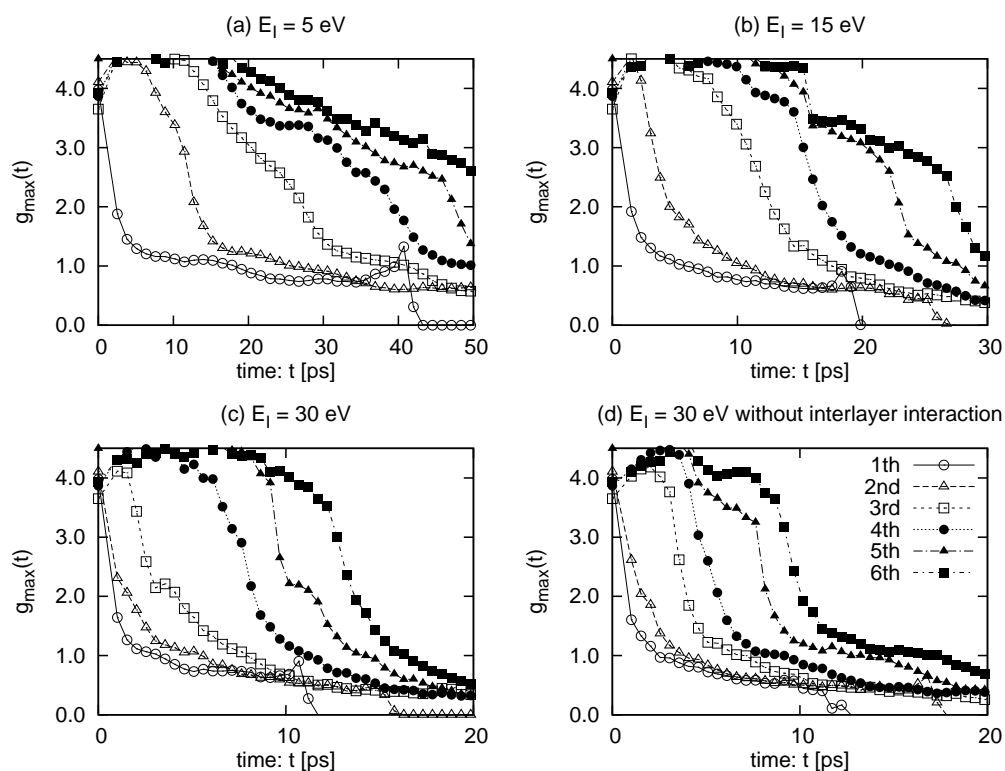


Figure 6: The maximum value of the radial distribution function $g_{\max}(t)$ for each graphene as a function of the time t . Only figure (d) is the result of the previous MD simulation without the interlayer intermolecular interaction.

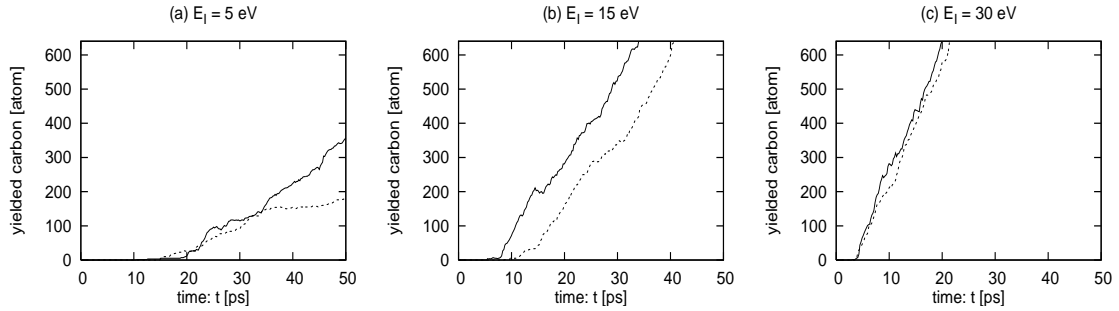


Figure 7: The erosion yields Y of the carbon atoms as a function of time. The solid lines are the erosion yields on the simulations using the interlayer intermolecular potential. The dashed lines are the erosion yields on the simulations without the interlayer intermolecular potential.

the graphite were reflected by the first graphene. When penetrating the graphene, the hydrogen atom passes through the six-membered ring. It is never seen that the hydrogen atom hits a carbon atom and ejects it from the graphene. Namely, physical sputtering did not occur.

In the cases that the incident energy were 15 eV and 30 eV, while the graphite surface maintained the graphene sheet structure, small hydrocarbon molecules, such as CH_x and C_2H_x , did not occur. However, for the incident energy of 5 eV, one C_2H_2 was generated keeping the first graphene flat (See Fig. 3(b)). After the atoms continued the above process, the first graphene was destroyed independent of the other graphenes.

In common with the incident energy, when the graphite was bombarded, the graphenes were destroyed one by one from the first graphene with time. To estimate the breakage of the graphite, a radial distribution function was calculated. Because there is no boundary in the z -direction, we cannot define the three dimensional volume in this simulation model. A two dimensional radial distribution function $g(r,t)$ of each graphene layer was defined. First, we defined $n_i(r,t)$ as the number of the carbon atoms which are located at a distance of less than r from the i -th carbon atom at time t . The average $n(r,t)$ is then given by

$$n(r,t) = \sum_i^{\text{layer}} \frac{n_i(r,t)}{160}, \quad (4.1)$$

where \sum_i^{layer} means summation in only one graphene. Consequently, the radial distribution function is given by

$$g(r,t) \equiv \frac{1}{4\pi r^2} \frac{dn(r,t)}{dr}. \quad (4.2)$$

We calculated this function for each graphene. We plotted the maximum values of the radial distribution function $g_{\text{max}}(t)$ as a function of time (see Fig. 6). These maximum

values often demonstrated the amount of the C-C bonds of length $r = 1.42 \text{ \AA}$ and correspond to the number of sp^2 bonds. The decrease of $g_{\max}(t)$ indicates the destruction of each graphene layer. As the incident energy increases, the speed of the decrease of $g_{\max}(t)$ increases. The decrease of $g_{\max}(t)$ of each graphene occurred at intervals.

Almost all of the yielded hydrocarbon molecules had chain structures like a C-C-C-C-H. Hydrogen atoms were located at the edge of the chain molecules. The chain molecules repeat chemical reactions out of the surface of the graphite. Because the chemical reactions changed the structures or length of the chain molecules, it was difficult that the yielded molecules were identified. To estimate the erosion yield $Y(t)$, we counted the number of carbon atoms that moved to the region $z > 24 \text{ \AA}$, where the first graphene is initially located on $z = 11.7 \text{ \AA}$. Fig. 7 shows the erosion yield $Y(t)$ as a function of time t . The erosion yield $Y(t)$ increases with time t linearly. As the incident energy increases, the speed of the increase of $Y(t)$ become faster.

5 Discussion

5.1 Dynamics of hydrogen atoms

Before the first graphene was broken, the behavior of hydrogen atoms depended on the incident energy. In the case of the incident energy of 5 eV, a lot of hydrogen atoms were adsorbed on the front of the first graphite. In the case of the incident energy of 15 eV, almost all of hydrogen atoms were reflected by the first graphene. In the case of the incident energy of 30 eV, the hydrogen atoms were adsorbed between the first and second graphene layers. The interlayer distance of the graphite was kept at about 3.35 \AA during those processes. Because the hydrogen atom and the graphene start chemical (strong) interaction at a distance less than 1.6 \AA , the hydrogen atom does not interact with two graphenes simultaneously. From this fact, we discuss the behavior of the hydrogen atoms comparing with the research of the interaction between a single hydrogen atom and a single graphene.

We had already researched the interaction between a single hydrogen atom and a single graphene using the MD simulation with modified Brenner REBO potential [14–16]. In that simulation, the hydrogen atom was injected into the graphene vertically. The interaction was classified into the three types, which are adsorption, reflection and penetration. Moreover, the adsorption on the backside of the graphene was distinguished from the adsorption on the front of the graphene. Since the injections were repeated tens of thousands of times while changing incident positions, we obtained the rates of the three types of the interactions. The rates of the three types of the interactions depend on the incident energy as follows: If the incident energy is less than 1 eV, almost all of the interactions become the reflection due to π -electron on the graphene surface. If the incident energy is 1 eV to 7 eV, the adsorption is dominant and has a peak at 5 eV. All of the adsorption in this range are on the front of graphene surface. If the incident energy is 7 eV to 30 eV, the reflection is dominant and has a peak at 15 eV. If the incident energy

is more than 30 eV, the penetration becomes dominant. To pass through the graphene, the hydrogen atom needs to expand the six-membered ring of the graphene. Moreover, if the incident energy is not sufficient to expand the six-membered ring and to leave the graphene, the hydrogen atom is adsorbed on the front or backside of the graphene. As a result, the rate of the adsorption has a small peak around 25 eV.

In the present MD simulation, the hydrogen atoms with 5 eV and 15 eV interact with the first graphene. Therefore, the adsorption and reflection in the MD simulation of 5 eV and 15 eV accord with the incident energy dependence of the interactions between a single hydrogen atom and a single graphene simply. In the case of the incident energy of 30 eV, the behavior of the hydrogen atom is derived from the combination of the three kinds of the interactions with the single graphene. The first interaction with the first graphene is similar to the penetration of the single graphene. When the hydrogen atom penetrates the first graphene, it reduces its kinetic energy. Because the incident energy is shifted to low energy, the next interaction with the second graphene becomes the reflection or adsorption with the single graphene. After that, the kinetic energy of the hydrogen atom is too small to penetrate the first graphene again. Consequently, the hydrogen atom stays in interlayer region. Because the loss of the kinetic energy due to the penetration depends on the injection point and timing, a few hydrogen atoms can penetrate the second graphene. If the hydrogen atom is injected by higher energy, it seems to go into deeper layers.

In addition, the rates of the interactions between a single hydrogen atom and a single graphene hardly depend on graphene temperature for the incident energy of more than 1 eV. This fact supports the above consideration even if the graphite is heated up due to the continuous injection in the present MD simulation.

5.2 Graphite peeling

We discuss the destruction of the graphite in this subsection. The animation of the MD simulation showed that the graphenes were peeled off one by one from the surface side (See Figs. 3, 4 and 5), which is called "graphite peeling". Moreover, the maximum values of the radial distribution function $g_{\max}(t)$ in Fig. 6 also imply this 'graphite peeling'. The maximum values of the radial distribution function $g_{\max}(t)$ show the amount of the sp^2 bonds. The decrease of $g_{\max}(t)$ corresponds to the destruction of the flat structure of the graphene. The graphite peeling is consistent with the tendency for $g_{\max}(t)$ of each graphene to decrease sequentially in Fig. 6.

On the other hand, in the previous MD simulation without the interlayer intermolecular interaction, which used only the modified Brenner REBO potential, the graphite peeling did not appear. The interlayer region was crushed by the pressure due to the injection of the hydrogen atoms. Namely, the graphenes were bound with the covalent bonds before being peeled. By comparison, we consider that because the repulsive force of the interlayer intermolecular interaction resisted the pressure due to the injection of the hydrogen atoms in the present MD simulation, the graphite could keep its layer structure.

Generally, we attach importance to the attractive force of the intermolecular interaction to produce the layer structure of the graphite. However, in the process of the bombardment on the graphite surface, the repulsive force of the intermolecular interaction played an important role to maintain the layer structure. Consequently, the graphenes were not connected by the covalent bonds and then they were peeled off one by one.

5.3 Erosion yield

In the case of the incident energy of 5 eV only, we observed just one C_2H_2 , which is regarded as the chemical sputtering maintaining the graphite structure (See Fig. 3(b)). However, the small hydrocarbon molecules, for example CH_x and C_2H_x , were hardly created until the occurrence of the graphite peeling. We consider that the incident energy flux is too high for the chemical sputtering on the clean graphite surface to occur. The graphite peeling seems to be melting of the graphene due to the increase of the kinetic energy.

During the graphite peeling, the yielded molecules often had the chain structures terminated by the hydrogen atoms. The erosion yield $Y(t)$ increased with time t linearly. This linearity process is namely regarded as steady state. The steady state accords with the fact that the graphenes were peeled off one by one. Of course, because the number of the graphite layers was finite, the steady state did not continue for a long time.

The present MD simulation achieved the steady state without the temperature control method which handles the kinetic energy of atoms. If the chemical sputtering on the experimental device involves the graphite peeling, the present MD simulation duplicates a real process. If the graphite peeling is not involved, the MD simulation needs the temperature control method to keep the graphite structure for a long time. However, the problem is not solved even if the temperature control method is used. The temperature control method usually causes rapid cooling because we have to finish a cooling process in the time scale of the MD simulation, which is at most nano-seconds. If the rapid cooling acts on the graphite surface directly, the movements of the atoms are restricted. Consequently, the chemical interaction on the graphite surface becomes far from the real process. If the temperature control method works in the region remote from the graphite surface, it cannot restrain the increase of the temperature of the graphite surface. Because the energy transport of the MD simulation has a realistic speed, which is caused by the realistic potential model, the energy was transferred from the graphite surface to the region of the temperature control method. We have to create a new method of the temperature control in the near future.

We make a comment on a flux of hydrogen atoms. The hydrogen atoms were injected every 0.1 ps in these simulations. The flux of hydrogen atoms corresponded to the $2.5 \times 10^{30} \text{ s}^{-1} \text{ m}^{-2}$. This was high flux compared with experimental values. However, in the present simulations, which treated the graphite of single crystal, energy due to the injection could be diffused in the graphene sheet. We know, from our previous works, that the energy due to the injection of a hydrogen atom could be eased in graphene sheet

within 0.1 ps. On the other hand, the graphite tiles used by experiments are a polycrystalline graphite. The polycrystalline graphite has lower speed of energy transport than that of the graphite of single crystal. Therefore, lower flux is required in the MD simulation treating the polycrystalline graphite. Moreover, if the flux of hydrogen atoms is close to experimental value, which is less than $10^{24} \text{ s}^{-1}\text{m}^{-2}$, we need to calculate 10^6 times as long as current MD simulations. That is to say, a high-speed simulation method is necessary.

Anyway, in the previous MD simulations without the interlayer interaction, no chemical sputtering was observed. Therefore, we have advanced one step toward real process in the present MD simulation.

6 Summary

The new potential model of the interlayer intermolecular interaction to represent "ABAB" stacking of the graphite was proposed. We performed the MD simulation of the bombardment of the hydrogen atoms on the graphite surface with the modified Brenner REBO potential and the interlayer intermolecular potential. We simulated the three cases of the incident energy of 5 eV, 15 eV or 30 eV. Before the first graphene was broken, the hydrogen atoms brought about the difference interaction process. In the case of the incident energy of 5 eV, many hydrogen atoms were adsorbed on the front of the first graphite. In the case of the incident energy of 15 eV, almost all of hydrogen atoms were reflected by the first graphene. In the case of the incident energy of 30 eV, the hydrogen atoms were adsorbed between the first and second graphenes. These processes are explained by the interaction between a single hydrogen atom and a single graphene. The maximum values of the radial distribution function $g_{\max}(t)$ and the animation of the MD simulation demonstrated that the graphenes were peeled off one by one. Because the repulsive force of the interlayer intermolecular interaction resisted the pressure due to the incident hydrogen atoms, the layer structure of the graphite was kept. The chemical sputtering of C_2H_2 was observed in only the case of the incident energy of 5 eV. During the graphite peeling, the yielded molecules often had the chain structures which are terminated by the hydrogen atoms. However, the small hydrocarbon molecules were not generated during the graphite peeling. The linear increase of the erosion yield $Y(t)$ was regarded as the steady state of the sputtering process.

Acknowledgments

The authors acknowledge stimulating discussion with Dr. Arimichi Takayama. The numerical simulations were carried out using the Plasma Simulator at the National Institute for Fusion Science. This work was supported in part by a Grand-in Aid for Exploratory Research (C), 2007, No. 17540384 from the Ministry of Education, Culture, Sports, Science and Technology. This work was also supported by National Institutes

of Natural Sciences undertaking for Forming Bases for Interdisciplinary and International Research through Cooperation Across Fields of Study, and Collaborative Research Programs (No. NIFS06KDAT012, No. NIFS06KTAT029, No. NIFS07USNN002 and No. NIFS07KEIN0091).

References

- [1] T. Nakano, H. Kubo, S. Higashijima, N. Asakura, H. Takenaga, T. Sugie, K. Itami, Nucl. Fusion 42 (2002) 689.
- [2] J. Roth, J. Nucl. Mater. 266–269 (1999) 51.
- [3] J. Roth, R. Preuss, W. Bohmeyer, S. Brezinsek, A. Cambe, E. Casarotto, R. Doerner, E. Gauthier, G. Federici, S. Higashijima, J. Hogan, A. Kallenbach, A. Kirschner, H. Kubo, J. M. Layet, T. Nakano, V. Philipps, A. Pospieszczyk, R. Pugno, R. Ruggieri, B. Schweer, G. Sergienko, M. Stamp, Nucl. Fusion 44 (2004) L21.
- [4] B. V. Mech, A. A. Haasz, J. W. Davis, J. Nucl. Mater. 241–243 (1997) 1147.
- [5] B. V. Mech, A. A. Haasz and J. W. Davis, J. Nucl. Mater. 255 (1998) 153.
- [6] A. Sagara, S. Masuzaki, T. Morisaki, S. Morita, H. Funaba, M. Goto, Y. Takamura, K. Nishimura, N. Noda, M. Shoji, H. Suzuki, A. Takayama, A. Komori, N. Ohyabu, O. Motojima, K. Morita, K. Ohya, J. P. Sharpe, LHD experimental group, J. Nucl. Mater. 313–316 (2003) 1.
- [7] C. Garcia and J. Roth, J. Nucl. Mater. 196–198 (1992) 573.
- [8] E. Salonen, K. Nordlund, J. Tarus, T. Ahlgren, J. Keinonen, C. H. Wu, Phys. Rev. B 60 (1999) R14005.
- [9] E. Salonen, K. Nordlund, J. Keinonen, C. H. Wu, Phys. Rev. B 63 (2001) 195415.
- [10] D. A. Alman, D. N. Ruzic, J. Nucl. Mater. 313–316 (2003) 182.
- [11] J. Marian, L. A. Zepeda-Ruiz, G. H. Gilmer, E. M. Bringaand, T. Rognlien, Phys. Scr. T 124 (2006) 65.
- [12] H. Nakamura, A. Ito, Mol. Sim. 33 (2007) 121.
- [13] A. Ito and H. Nakamura, to be published in Thin Solid Films, (cond-mat/0709.2976).
- [14] A. Ito, H. Nakamura, J. Plasma Phys. 72 (2006) 805.
- [15] A. Ito, H. Nakamura, A. Takayama, submitted, (cond-mat/0703377).
- [16] H. Nakamura, A. Takayama and A. Ito, Contrib. Plasma Phys. 48 (2008) 265.
- [17] D. W. Brenner, O. A. Shenderova, J. A. Harrison, S. J. Stuart, B. Ni, S. B. Sinnott, J. Phys.: Condens. Matter 14 (2002) 783.
- [18] P. M. Morse, Phys. Rev. 34 (1929) 57.
- [19] G. C. Abell, Phys. Rev. B 31 (1985) 6184.
- [20] J. Tersoff, Phys. Rev. B 37 (1988) 6991.
- [21] J. Tersoff, Phys. Rev. B 39 (1989) 5566; 41 (1990) 3248(E).
- [22] D. W. Brenner, Phys. Rev. B 42 (1990) 9458; 46 (1992) 1948(E).
- [23] M. Hasegawa and K. Nishidate, Phys. Rev. B 70 (2004) 205431.
- [24] H. -P. Boehm, R. Setton, E. Syumpp, Pure & Appl. Chem. 66 (1994) 1893.
- [25] M. Suzuki, J. Math. Phys. 26 (1985) 601.